

FE/FMBE coupling to model fluid–structure interaction

S. Schneider^{*,†}

CNRS/LMA, 31 Chemin Joseph-Aiguier, 13402 Marseille Cedex 20, France

SUMMARY

In this paper, a finite element (FE)/fast multipole boundary element (FMBE)-coupling method is presented for modeling fluid–structure interaction problems numerically. Vibrating structures are assumed to consist of elastic or sound absorbing materials. An FE method (FEM) is used for this part of the solution. This structural sub-domain is embedded in a homogeneous fluid. The case where the boundary of the structural sub-domain has a very complex geometry is of special interest. In this case, the BE method (BEM) is a more suitable numerical tool than FEM to account for the sound propagation in the homogeneous fluid. The efficiency of the BEM is increased by using FMBEM. The BE-surface mesh required is directly generated by the FE-mesh used to discretize the structural sub-domain and the absorbing material. This FE/FMBE-coupling method makes it possible to predict the effects of arbitrarily shaped absorbing materials and vibrating structures on the sound field in the surrounding fluid numerically. The coupling method proposed is used to study the acoustic behavior of the lining of an anechoic chamber and that of an entire anechoic chamber in the low-frequency range. The numerical results obtained are compared with the experimental data. Copyright © 2008 John Wiley & Sons, Ltd.

Received 12 September 2007; Revised 29 April 2008; Accepted 13 May 2008

KEY WORDS: fluid–structure coupling; FEM; BEM; fast multipole method; absorbing materials

1. INTRODUCTION

This paper deals with the numerical treatment of the interaction between vibrating structures, absorbing materials and an ambient fluid in the frequency domain. Special attention is paid to the case where the fluid domain is unbounded or where it is enclosed by a boundary with a complex shape, due to either the special shape of the absorbing material used to control its acoustic properties or the presence of arbitrarily shaped and/or multiple radiators and scatterers.

The finite element method (FEM) is a numerical tool, which is commonly used to solve structural [1] and acoustical [2] problems in many fields of engineering. Sound absorbing materials

*Correspondence to: S. Schneider, CNRS/LMA, 31 Chemin Joseph-Aiguier, 13402 Marseille Cedex 20, France.

†E-mail: schneider@lma.cnrs-mrs.fr

Contract/grant sponsor: German Research Foundation

are generally modeled using Biot's theory [3, 4], which takes the material to have two phases, i.e. a solid phase and a fluid phase. Numerical implementations are performed using either a displacement formulation [5] for both phases ($\{u, U\}$ -formulation) or a displacement–pressure formulation ($\{u, p\}$ -formulation) [6] along with the FEM. Boundary element (BE) approaches have also been recently proposed in [7, 8]. Structural and fluid sub-domains are often handled using FEM, and this coupling is often referred to as finite element FE/FE coupling [9, 10]. The FEM requires the structural and fluid sub-domains to be meshed so that the meshes match at the fluid/structure interface unless mortar coupling techniques are applied [11]. The meshing of the fluid sub-domains is not always easy to manage when dealing with sound propagation in unbounded domains and/or radiation or scattering problems with several scatterers or radiators. Even infinite elements [12, 13] require the meshing of an intermediate three-dimensional fluid domain. The FE/FE-coupling approach therefore has its limitations. The meshing of the ambient fluid domain Ω_{BE} can be avoided by using the BE method (BEM) [14] for the numerical treatment of sound propagation in the homogeneous fluid. This approach yields the FE/BE coupling [15–18]. An FE/BE-coupling method of studying the behavior of flat panels made of an absorbing material was recently presented [19]. However, the BEM has rarely been applied so far to simulate fluid–structure interaction problems involving geometries of industrial interest, mainly due to the numerical complexity of $\mathcal{O}(N^2)$ for a problem with N unknowns. During the last few years, various strategies have been developed to overcome this drawback of BEM. One approach consists in using a suitable wavelet basis together with a drooping strategy to sparsify the dense matrix [20]. The most challenging part of this approach is the direct evaluation of the matrix in the wavelet basis. A second approach consists in finding a low-rank approximation of the dense matrix and using efficient \mathcal{H} -matrix techniques [21, 22]. An approximation of the fundamental solution forms the basis of methods such as the regular grid method [23], panel clustering [24] and the fast multipole method (FMM) [25]. In this study, an FM-accelerated BEM (FMBEM) with a complexity of $\mathcal{O}(N \log^2 N)$ was used. The greater efficiency of the BEM makes it possible to solve large-scale fluid–structure interaction problems involving arbitrarily shaped geometries using the FE/FMBEM-coupling procedure presented in [11]. Here we extend this approach by also dealing with sound absorbing materials and their interactions with vibrating structures and the ambient fluid.

This paper is structured as follows. Sections 2 and 3 review the application of the FEM and the BEM to solving the differential equations in the sub-domains. The coupling between the sub-domains is addressed in Section 4. Some aspects of the numerical implementation are presented in Section 5. The numerical results obtained are compared with the experimental data in Section 6.

2. FE SUB-DOMAIN

This study deals with the coupling of vibrating structures, absorbing materials and acoustic fluids. Figure 1 shows a schematic diagram of the arrangement and the notation of the sub-domains adopted here. The sub-domain Ω_S denotes the domain occupied by a given mechanical structure. The sub-domain occupied by sound absorbing materials or acoustic fluids is referred to as Ω_B and Ω_F , respectively. The symbol Γ_A denotes the boundary of the domain Ω_A . A common boundary between two sub-domains Ω_A and Ω_B is referred to as Γ_{A-B} . Pressure and displacement boundary conditions are imposed on Γ_{S-p^0} and Γ_{S-u^0} , respectively. Each of the sub-domains Ω_S , Ω_B and Ω_F may itself consist of several sub-domains of the same type, but having different material properties.

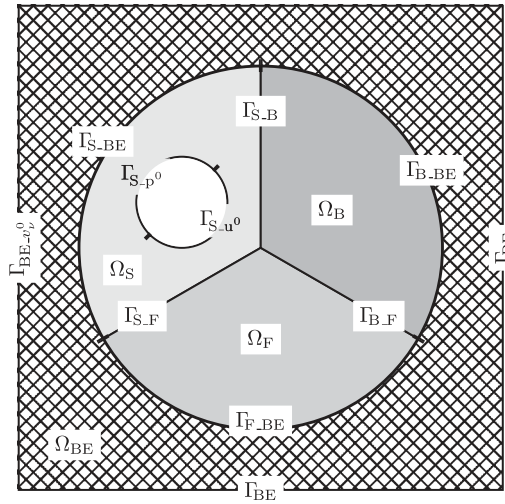


Figure 1. Definition of the sub-domains and their boundaries.

Only the sub-domain Ω_{BE} is a fluid sub-domain occupied by a given homogeneous and isotropic fluid. Therefore in what follows, the distinction will be made between the fluid sub-domains Ω_F and Ω_{BE} . We focus on a general description of fluid–structure coupling problems and therefore no special restrictions are made about the geometry, boundary conditions or material behavior. Under these general conditions, the FEM is the most suitable numerical method of solving the governing differential equations in the sub-domains Ω_S , Ω_B and Ω_F . The application of the FEM to solving these differential equations will be briefly reviewed. For further details, see [1, 6].

In this study, we focus on the behavior of elastic structures undergoing small displacements and deformations. The displacement field u^s of the structure in the sub-domain Ω_S can therefore be expressed as the solution of

$$\nabla \cdot \sigma^s + \omega^2 \tilde{\rho}_S u^s = 0 \tag{1}$$

with the elastic stress tensor σ^s . The term $\tilde{\rho}_S$ denotes a complex-valued density of the elastic material. This generalization was introduced to model the viscous dissipation effects of the material. Using the admissible variation δu^s of the structural displacement u^s and integrating Equation (1) multiplied by δu^s by part leads to the variational formulation

$$\int_{\Omega_S} \sigma^s : \varepsilon^s(\delta u^s) d\Omega - \omega^2 \tilde{\rho}_S \int_{\Omega_S} u^s \cdot \delta u^s d\Omega - \int_{\Gamma_S} \delta u^s \cdot \sigma_v^s d\Gamma = 0 \tag{2}$$

where σ_v^s denotes the vector of the normal stresses on the boundary Γ_S of the structural sub-domain Ω_S .

The mechanical behavior and sound propagation in the domain Ω_B occupied by sound absorbing porous materials were modeled using Biot’s theory [3, 26]. Biot originally developed this model for studying sound propagation in sediments. Under the assumption that the wavelength in the material is much larger than the characteristic size of the material’s micro-structure, i.e. the pores, a porous material can be taken to be a homogeneous material consisting of a solid and a fluid

phase coupled by a volumetric coupling. In the context of sound absorbing materials, the solid phase is often referred to as the frame of the material. Biot developed a set of differential equations for the unknown displacement field u^b of the solid phase of the material and the displacement field U^f of the fluid phase. In the frequency domain, an equivalent but numerically more efficient formulation in terms of the variables $\{u^b, p^b\}$ was developed by Atalla [6]. Using this formulation, the displacement field u^b of the frame and the sound pressure p^b of the fluid phase of the porous material are the solutions of the following set of differential equations:

$$\nabla \cdot \sigma^b + \omega^2 \tilde{\rho} u^b + \gamma \nabla p^b = 0 \quad (3)$$

$$\Delta p^b + \frac{\omega^2 \tilde{\rho}_{22}}{\tilde{R}} p^b - \frac{\omega^2 \tilde{\rho}_{22}}{h^2} \gamma \nabla \cdot u^b = 0 \quad (4)$$

To account for the dissipation effects at work in the pores of the material over a wide frequency range, the use of a frequency-dependent viscous damping factor (see [26, 27]) and a frequency-dependent compressibility modulus of the fluid phase (see [28]) have been proposed in the literature. Depending on the form of the pores, which is represented by the characteristic viscous length Λ and the characteristic thermal length Λ' , and the viscosity of the fluid, the authors developed frequency-dependent complex-valued functions to express this dependency. In this study

$$\tilde{b} = \sigma h^2 \left(1 + j \frac{4\alpha_\infty^2 \eta \rho^f}{\sigma^2 \Lambda^2 h^2} \omega \right)^{1/2}$$

was used for the viscous damping factor and

$$\tilde{R}(\omega) = h \frac{K_0}{\gamma - (\gamma - 1) \left[1 + \frac{8\eta}{j\omega \Lambda'^2 B^2 \rho^f} \left(1 + j\rho^f \frac{\Lambda'^2 B^2 \omega}{16\eta} \right)^{1/2} \right]^{-1}}$$

was used for the compressibility modulus of the fluid phase, as proposed in [4]. K_0 denotes the adiabatic bulk modulus, η is the viscosity, γ is the ratio between the specific heat per unit mass at constant pressure and constant volume and B^2 is the Prandtl number of the fluid. In addition, the following abbreviations

$$\begin{aligned} \tilde{\rho}_{11} &= (1-h)\rho^s + h(\alpha_\infty - 1)\rho^f - j\frac{\tilde{b}}{\omega}, & \tilde{\rho}_{22} &= h\alpha_\infty\rho^f - j\frac{\tilde{b}}{\omega} \\ \tilde{\rho}_{12} &= -h(\alpha_\infty - 1)\rho^f + j\frac{\tilde{b}}{\omega}, & \tilde{\rho} &= \tilde{\rho}_{11} - \frac{\tilde{\rho}_{12}^2}{\tilde{\rho}_{22}} \\ \gamma &= h \left(\frac{\tilde{\rho}_{12}}{\tilde{\rho}_{22}} - \frac{1-h}{h} \right) \end{aligned}$$

have been used, where ρ^s stands for the density of the frame material, ρ^f for the fluid density, h for the porosity, α_∞ for the tortuosity and σ for the flow resistivity of the absorbing material. Tilded variables indicate complex variables with the complex unit $j = \sqrt{-1}$. For a more detailed description of the Biot model and the notation used, see [3, 6, 26].

A variational formulation of the governing differential equations involving the admissible variations δu^b and δp^b of displacement u^b and the pressure p^b leads to

$$\int_{\Omega_B} \sigma^b : \varepsilon^b(\delta u^b) d\Omega - \omega^2 \tilde{\rho} \int_{\Omega_B} u^b \cdot \delta u^b d\Omega - \gamma \int_{\Omega_B} \delta u^b \cdot \nabla p^b d\Omega - \int_{\Gamma_B} \delta u^b \cdot \nu p^b d\Gamma - \int_{\Gamma_B} \delta u^b \cdot \nu \cdot \sigma^t d\Gamma = 0 \quad (5)$$

$$\frac{h^2}{\omega^2 \tilde{\rho}_{22}} \int_{\Omega_B} \nabla \delta p^b \cdot \nabla p^b d\Omega - \frac{h^2}{\tilde{R}} \int_{\Omega_B} \delta p^b p^b d\Omega - \gamma \int_{\Omega_B} \nabla \delta p^b \cdot u^b d\Omega - \int_{\Gamma_B} \delta p^b \nu \cdot u^t d\Gamma = 0 \quad (6)$$

where ν denotes the outward normal vector. In the above equations, the total stress tensor $\sigma^t = \sigma^b - hIp^b$ and the vector of the total displacement $u^t = (1-h)u^b + hU^f$ were introduced to simplify the coupling between the sub-domains.

Sound propagation in the fluid domain Ω_F was modeled using the time harmonic Helmholtz equation [29]

$$\Delta p^f + \frac{\omega^2 \rho^f}{R} p^f = 0 \quad (7)$$

with the bulk modulus $R = K_0$ of the fluid. This notation was introduced to show the equivalence between Equations (4) and (7) in the case where the frame of the absorbing material is assumed to be motionless. In this situation, we have $u^b \equiv 0$ and Equation (4) reduces to

$$\Delta p^b + \frac{\omega^2 \tilde{\rho}_{22}}{\tilde{R}} p^b = 0$$

which can be interpreted similar to the Helmholtz equation for a fluid with dissipation. This model is often referred to as the equivalent fluid model. Again using the admissible pressure δp^f , the variational formulation of Equation (7) reads

$$\frac{1}{\omega^2 \rho^f} \int_{\Omega_F} \nabla \delta p^f \cdot \nabla p^f d\Omega - \frac{1}{R} \int_{\Omega_F} \delta p^f p^f d\Omega - \frac{1}{j\omega} \int_{\Gamma_F} \delta p^f v_\nu d\Gamma = 0 \quad (8)$$

with the normal velocity v_ν of the fluid at the boundary Γ_F of the fluid sub-domain Ω_F .

The variational formulations presented above form the basis of FEM. The unknown variables were discretized using hierarchic basis functions based on Legendre polynomials [30]. These basis functions make it possible to efficiently use basis functions of different polynomial degrees on a given FE-mesh and therefore provide a very flexible numerical tool.

3. BE SUB-DOMAIN

The FEM has proved to be a highly efficient means of solving sound propagation problems of practical interest. However, this method becomes less efficient with unbounded or complex-shaped fluid domains. CAD-software often gives geometric models that can be used in a subsequent FE-analysis for the structural sub-domains. As the geometry of the ambient fluid is often only given implicitly as the complement to the structural sub-domain, the resulting geometric models are not

adapted to FE-meshing and a fine spatial discretization is necessary to model the geometry without defeaturing. In addition, these geometries must often be meshed with tetrahedral elements that require quadratic basis functions. The latter lead to FE-matrices with a relatively large bandwidth, which reduces the efficiency of numerical algorithms.

To avoid having to mesh the domain Ω_{BE} , the BEM provides an alternative to the FEM in this specific situation, as the BEM requires only a geometric model for the boundary Γ_{BE} , which is implicitly given by the boundaries of the domains Ω_S , Ω_B and Ω_F , see Figure 1. Contrary to what is illustrated in this figure, the boundaries Γ_{S_BE} , Γ_{B_BE} and Γ_{F_BE} are assumed to have a complex shape. $\Gamma_{BE_v^0}$ denotes a boundary where a normal surface velocity is prescribed.

Instead of using the variational formulation equation (8) of the time harmonic Helmholtz equation as the starting point of the numerical treatment of the sound propagation in the surrounding fluid, the boundary integral representation of the solution of the time harmonic Helmholtz equation (7) was used here. The scattered or radiated sound field p^s of an object can be described in terms of its boundary data [31] as

$$c(y)p^s(y) + \int_{\Gamma_{BE}} \frac{\partial \phi(x, y)}{\partial v} p^s(x) d\Gamma_{BE} - \int_{\Gamma_{BE}} \phi(x, y) \frac{\partial p^s(x)}{\partial v} d\Gamma_{BE} = 0 \quad (9)$$

with the fundamental solution

$$\phi(x, y) = \frac{e^{jk|x-y|}}{4\pi|x-y|} = \frac{e^{jkr}}{4\pi r}, \quad r = |x-y|, \quad x \neq y \quad (10)$$

of the Helmholtz equation in three dimensions and the wave number $k = \omega/\sqrt{R/\rho^f}$. This approach avoids the need to mesh the three-dimensional fluid domain Ω_{BE} . When applied to exterior problems, i.e. sound propagation in an unbounded domain, Equation (9) has non-unique solutions when the wave number k is equal to an eigenvalue of the corresponding interior problem. This non-uniqueness has no physical meaning. To obtain a unique solution of the exterior problem at all wave numbers k , Burton and Miller [32] have suggested the use of a linear combination of Equation (9) and its normal derivative

$$c(y)p^s(y) + \int_{\Gamma_{BE}} \frac{\partial \phi(x, y)}{\partial v_x} p^s(x) d\Gamma_{BE} - \int_{\Gamma_{BE}} \phi(x, y) \frac{\partial p^s(x)}{\partial v_x} d\Gamma_{BE} \\ + \alpha \left(c(y) \frac{\partial p^s(y)}{\partial v_y} + \int_{\Gamma_{BE}} \frac{\partial^2 \phi(x, y)}{\partial v_x \partial v_y} p^s(x) d\Gamma_{BE} - \int_{\Gamma_{BE}} \frac{\partial \phi(x, y)}{\partial v_y} \frac{\partial p^s(x)}{\partial v_x} d\Gamma_{BE} \right) = 0 \quad (11)$$

involving the coupling parameter α . These authors have shown that for a coupling parameter α with $\Im(\alpha) > 0$, the above equation has a unique solution for all wave numbers k . A value of $\alpha = j/k$ has been recommended in the literature, see [33]. When dealing with interior problems, the parameter α is set to zero. Another version of the Burton/Miller approach, which avoids the need to use the hyper-singular operator, can be found in [34].

In the present context, the sub-domain Ω_{BE} will be coupled to the FE sub-domains Ω_S , Ω_B and Ω_F . For this purpose, it is advantageous to replace the scattered sound field p^s by the total sound field $p = p^s + p^{inc}$, which is the sum of the scattered field and a given sound field p^{inc} . Assuming

in addition that the normal surface velocity v_v , defined as

$$v_v = \frac{1}{a} \frac{\partial p}{\partial v}$$

with $a = j\omega\rho^f$, is given at the boundary $\Gamma_{BE-v_v^0}$, Equation (9) can be rewritten as follows:

$$\begin{aligned} c(y)p(y) + \int_{\Gamma_{BE}} \frac{\partial\phi(x,y)}{\partial v_x} p(x) d\Gamma_{BE} - a \int_{\Gamma_{BE} \setminus \Gamma_{BE-v_v^0}} \phi(x,y)v_v(x) d\Gamma_{BE} \\ = c(y)p^{inc}(y) + \int_{\Gamma_{BE}} \frac{\partial\phi(x,y)}{\partial v_x} p^{inc}(x) d\Gamma_{BE} - a \int_{\Gamma_{BE} \setminus \Gamma_{BE-v_v^0}} \phi(x,y) \frac{\partial p^{inc}}{\partial v} d\Gamma_{BE} \\ + a \int_{\Gamma_{BE-v_v^0}} \phi(x,y)v_v^0(x) d\Gamma_{BE} \end{aligned} \tag{12}$$

All unknown quantities are collected on the left-hand side of Equation (12) and the right-hand side contains the loading term. For numerical implementations, either Equation (12) or a linear combination of Equation (12) and its normal derivative must be discretized. A collocation method with discontinuous basis functions [35–37], where the unknown quantities are interpolated at the collocation points y_j , has been used to obtain a system of linear equations

$$Hp - Gv_v = r_{BE}^0 \tag{13}$$

for the vectors of the unknown pressure p and normal velocity v_v at the boundary Γ_{BE} . The use of these discontinuous basis functions shows better numerical properties as it has been shown in the above-mentioned publications. Especially when using the Burton/Miller approach having the collocation points inside the element is very important as the condition $\Gamma_{BE} \in C^1$ must be met at each collocation point y_j . As sound pressure and velocity at the nodes inside the elements are used for interpolation and collocation the correct number of BE equations is obtained, however. Owing to the use of discontinuous basis functions, the function $c(y)$ in Equation (12) takes the constant value $c = 0.5$, as we have $\Gamma_{BE} \in C^1$ at each collocation point y_j . Collocation points were placed at the center of the element when constant basis functions were used and at points corresponding to the zeros of the Legendre polynomial of order 2 when linear basis functions were used. The right-hand side r_{BE}^0 of Equation (13) is given by

$$r_{BE}^0 = Hp^{inc} + \frac{1}{a} G \frac{\partial p^{inc}}{\partial v} - Gv_v^0 \tag{14}$$

and this equation accounts for a given incident sound field p^{inc} and a given surface velocity v_v^0 at $\Gamma_{BE-v_v^0}$. The matrices H and G are defined as

$$H = \frac{1}{2}I + \int_{\Gamma_{BE}} \left(\frac{\partial\phi(x,y)}{\partial v_x} + \alpha \frac{\partial^2\phi(x,y)}{\partial v_y \partial v_x} \right) \Phi^{BE} d\Gamma_{BE} \tag{15}$$

$$G = \alpha \frac{1}{2}aI - a \int_{\Gamma_{BE}} \left(\phi(x,y) + \alpha \frac{\partial\phi(x,y)}{\partial v_y} \right) \Phi^{BE} d\Gamma_{BE} \tag{16}$$

where Φ^{BE} denotes the matrix containing the BE-basis functions.

A well-known disadvantage of BEM is the fact that the above matrices H and G are fully populated, which causes the $\mathcal{O}(N^2)$ complexity of this numerical method when dealing with a problem with N unknowns. During the last few years, several techniques [20–25] have been proposed to reduce this complexity. The FMM seems to be the most widely adopted method. An overview of the state of the art of the FMM can be found in [38]. The main idea of FMM is to approximate the fundamental solution (10) for points x and y with $|x - y| > \rho > 0$ in terms of spherical Hankel functions $h_l^{(1)}$, Legendre polynomials P_l and plane waves (see [39]). The remaining points form the near-field part of the fundamental solution where standard BEM-techniques must be applied. For numerical implementations, clusters τ_i with the center z_i and the radius ρ_i are introduced so that each point $y \in \Gamma_{\text{BE}}$ can be assigned to a cluster τ_i . Thereafter, for two well-separated points $x \in \tau_i$ and $y \in \tau_j$, satisfying $|(z_j - y) + (x - z_i)| < |z_j - z_i|$, the fundamental solution (10) and its normal derivative can be approximated as follows:

$$\begin{aligned}\phi(x, y) &\approx \frac{jk}{4\pi} \int_{\mathbb{S}^2} e^{jk(y-z_j) \cdot \hat{s}} \mu^M(z_j - z_i, \hat{s}) e^{jk(z_i-x) \cdot \hat{s}} d\omega(\hat{s}) \\ \nabla_x \phi(x, y) \cdot \nu_x &\approx \frac{k^2}{4\pi} \int_{\mathbb{S}^2} e^{jk(y-z_j) \cdot \hat{s}} \mu^M(z_j - z_i, \hat{s}) \hat{s} \cdot \nu_x e^{jk(z_i-x) \cdot \hat{s}} d\omega(\hat{s})\end{aligned}$$

where the function $\mu^M(z_j - z_i, \hat{s})$ denotes the truncated translation operator

$$\mu^M(z_j - z_i, \hat{s}) = \frac{1}{4\pi} \sum_{l=0}^M (2l+1) j^l h_l^{(1)}(k|z_j - z_i|) P_l(\hat{s} \cdot \widehat{(z_j - z_i)}) \quad (17)$$

of the FMM with the truncation index M . For further details about the FMM and the numerical implementation, see [38, 40]. Using FMM, matrices H and G now read as

$$\begin{aligned}H &= H_{\mathcal{N}} + H_{\mathcal{F}} \approx H_{\mathcal{N}} + SDT^H \\ G &= G_{\mathcal{N}} + G_{\mathcal{F}} \approx G_{\mathcal{N}} + SDT^G\end{aligned}$$

The sparse matrices $H_{\mathcal{N}}$ and $G_{\mathcal{N}}$ represent the near-field part of H and G , respectively. They are evaluated using standard BE techniques. Matrices S , D , T^H and T^G arising from the series expansion are also sparse matrices. For the definition of matrices $H_{\mathcal{N}}$, $G_{\mathcal{N}}$, S , D , T^H and T^G , see [41]. Applying FMM on a hierarchy of clusters reduces the complexity of BEM from $\mathcal{O}(N^2)$ to $\mathcal{O}(N \log^2 N)$ [40]. This improvement makes the BEM efficiently applicable to real-life radiation and scattering problems [11].

4. COUPLING BETWEEN THE SUB-DOMAINS

The governing equations shown above are linked up via continuity conditions across the common boundaries of the sub-domains.

At the common boundary Γ_{S_B} between the structural sub-domain Ω_{S} and the sub-domain Ω_{B} occupied by the absorbing material, the continuity of the displacement fields and the normal stresses requires that

$$\begin{aligned}u^{\text{s}} &= u^{\text{b}} \\ \nu \cdot \sigma^{\text{s}} &= -\nu \cdot \sigma^{\text{t}}\end{aligned}$$

holds true. Coupling a structural sub-domain Ω_S with a fluid sub-domain Ω_F imposes the continuity of the normal stresses and the normal surface velocity

$$\begin{aligned} v \cdot \sigma^s &= -v p^f \\ j\omega v \cdot u^s &= -v_v \end{aligned}$$

at the boundary Γ_{S_F} . At the interface Γ_{B_F} between an absorbing material and a fluid domain, we impose (see [42]) the continuity of the normal stresses and the normal surface velocities, as well as the continuity of the pressure

$$\begin{aligned} v \cdot \sigma^t &= -v p^f \\ j\omega v \cdot u^t &= -v_v \\ p^b &= p^f \end{aligned}$$

As the basis functions differ between the FE- and BE-sub-domains, the continuity of the sound pressure and the normal velocity cannot be ensured by simply identifying the corresponding unknowns. In this study, we impose the continuity averaged over the surface of each element. To shorten the notation the symbol u^{FE} was used for all displacement degrees of freedom, the symbol p^{FE} was used for pressure degrees of freedom in the finite element sub-domains, the symbol p^{BE} was used for pressure degrees of freedom in the BE sub-domain and the symbol v^{BE} was used for velocity degrees of freedom in the BE sub-domain. The continuity condition for the sound pressure on the common boundary $\Gamma_{B_{BE}}$ between the sub-domains Ω_B and Ω_{BE} and on the common boundary $\Gamma_{F_{BE}}$ between the sub-domains Ω_F and Ω_{BE} therefore reads

$$0 = \int_{\Gamma_{BF_{BE}}} \Phi^{BE T} (\Phi^{BE} p^{BE} - \Phi_p^{FE} p^{FE}) d\Gamma = \underbrace{\int_{\Gamma_{BF_{BE}}} \Phi^{BE T} \Phi^{BE} d\Gamma}_{=: S_p} p^{BE} - \underbrace{\int_{\Gamma_{BF_{BE}}} \Phi^{BE T} \Phi_p^{FE} d\Gamma}_{=: C_{BE}^{BE T}} p^{FE}$$

where Φ_p^{FE} denotes the matrix of the FEM basis functions that approximate the sound pressure and $\Gamma_{BF_{BE}} = \Gamma_{B_{BE}} \cap \Gamma_{F_{BE}}$ denotes the common boundary of Ω_B , Ω_F and Ω_{BE} . Hence, the sound pressure p^{BE} at $\Gamma_{BF_{BE}}$ is given by the sound pressure p^{FE} as follows:

$$p^{BE}|_{\Gamma_{BF_{BE}}} = S_p^{-1} C_{BE}^{BE T} p^{FE}$$

Similarly, at the common boundary $\Gamma_{S_{BE}}$ of the sub-domains Ω_S and Ω_{BE} we have

$$\begin{aligned} 0 &= \int_{\Gamma_{S_{BE}}} \Phi^{BE T} (\Phi^{BE} v^{BE} + j\omega v \cdot \Phi_u^{FE} u^{FE}) d\Gamma \\ &= \underbrace{\int_{\Gamma_{S_{BE}}} \Phi^{BE T} \Phi^{BE} d\Gamma}_{=: S_v} v^{BE} + j\omega \underbrace{\int_{\Gamma_{S_{BE}}} \Phi^{BE T} v \cdot \Phi_u^{FE} d\Gamma}_{=: C_{BE}^{S T}} u^{FE} \end{aligned}$$

and the normal velocity v^{BE} on $\Gamma_{S_{BE}}$ can be expressed as a function of the displacement u^{FE}

$$v^{BE}|_{\Gamma_{S_{BE}}} = -j\omega S_v^{-1} C_{BE}^{S T} u^{FE}$$

where Φ_u^{FE} contains the FEM basis functions approximating the displacement field. When using the method presented here for coupling the sub-domains, the kind of sub-domain in contact with the boundary Γ_{BE} at a specific point determines whether the sound pressure or the normal surface velocity is the unknown variable in the BEM. At $\Gamma_{\text{S_BE}}$, the sound pressure p^{BE} is the unknown variable, whereas the normal surface velocity is given by the normal displacement of the structure via the above coupling conditions. In cases where the boundary Γ_{BE} is in contact with either Ω_{B} or Ω_{F} , then the normal velocity v^{BE} will be the unknown variable and the sound pressure will be given by the finite element discretization via the above interpolation matrix $S_p^{-1} C_{\text{BE}}^{\text{BF}^T}$. Because of the discontinuous basis functions used, matrices S_p and S_v are block-diagonal matrices with a block size of 1 when constant basis functions are used and a block size of 4 when linear basis functions are used.

5. NUMERICAL IMPLEMENTATION

We will now briefly outline some of the general aspects involved in the numerical implementation of the proposed FE/FMBEM-coupling method. For further details about the evaluation of the FE-matrices and their assembly, see [1].

For the structural sub-domain Ω_{S} , in addition to the stiffness and mass matrices \tilde{C}_{S} and M_{S} , the matrices C_{F}^{S} and C_{BE}^{S} resulting from the coupling conditions must also be evaluated to obtain the matrix equation

$$[\tilde{C}_{\text{S}} - \omega^2 \tilde{\rho}_{\text{S}} M_{\text{S}}] u_{\text{S}}^{\text{FE}} + C_{\text{F}}^{\text{S}} p_{\text{F}}^{\text{FE}} + C_{\text{BE}}^{\text{S}} p^{\text{BE}} = f^n - C_{\text{S_p}^0}^{\text{S}} p^0 = r_{\text{FE}}^0$$

for the unknown displacement u_{S}^{FE} and pressures p_{F}^{FE} and p^{BE} . A complex-valued, possibly frequency-dependent stiffness matrix \tilde{C}_{S} that accounts for the dissipation effects occurring in the vibrating structure has been used. Vectors f^n and p^0 account for the given nodal forces and surface loads acting on the vibrating structure. As we assumed that there are no such loads in Ω_{B} and Ω_{F} , we have the following expressions:

$$\begin{aligned} & [\tilde{C}_{\text{BS}} - \omega^2 \tilde{\rho}_{\text{B}} M_{\text{BS}}] u_{\text{B}}^{\text{FE}} - \gamma C_{\text{BF}}^{\text{BS}} p_{\text{B}}^{\text{FE}} - M_{\text{B}}^{\text{S}} p_{\text{B}}^{\text{FE}} = 0 \\ & -\gamma C_{\text{BF}}^{\text{BS}^T} u_{\text{B}}^{\text{FE}} - M_{\text{B}}^{\text{S}^T} u_{\text{B}}^{\text{FE}} + \left[\frac{h^2}{\omega^2 \tilde{\rho}_{22}} C_{\text{BF}} - \frac{h^2}{R} M_{\text{BF}} \right] p_{\text{B}}^{\text{FE}} + \frac{1}{j\omega} C_{\text{BE}}^{\text{BF}} v^{\text{BE}} = 0 \end{aligned}$$

for the unknown displacement u_{B}^{FE} and the pressure p_{B}^{FE} in Ω_{B} . In addition to the stiffness and mass matrices \tilde{C}_{BS} , C_{BF} , M_{BS} and M_{BF} , the matrix $C_{\text{BF}}^{\text{BS}}$ must be evaluated. This matrix corresponds to the discretization of the volumetric coupling condition, the third term on the left-hand side of Equations (5) and (6), between the two phases of the porous material. Matrices M_{B}^{S} and $C_{\text{BE}}^{\text{BF}}$ result from the coupling conditions when Ω_{B} is in contact either with Ω_{S} or Ω_{BE} , respectively. For the fluid sub-domain Ω_{F} , it follows that

$$C_{\text{F}}^{\text{S}^T} u_{\text{S}}^{\text{FE}} + \left[\frac{1}{\omega^2 \tilde{\rho}_{\text{F}}} C_{\text{F}} - \frac{1}{R} M_{\text{F}} \right] p_{\text{F}}^{\text{FE}} + \frac{1}{j\omega} C_{\text{BE}}^{\text{F}} v^{\text{BE}} = 0$$

with the unknown surface velocity v^{BE} at $\Gamma_{\text{B_BE}}$ and $\Gamma_{\text{B_F}}$. The matrix C_{BE}^{F} denotes the coupling condition on the common boundary between the fluid sub-domain Ω_{F} and the sub-domain Ω_{BE} .

Finally, at Γ_{BE} we have

$$H(p^{BE} + S_p^{-1} C_{BE}^{BF^T} p^{FE}) - G(v^{BE} - j\omega S_v^{-1} C_{BE}^{S^T} u_S^{FE}) = r_{BE}^0$$

with the same coupling matrices as above.

After grouping the unknowns and collecting all the matrices belonging to displacement degrees of freedom into the matrix A^{uu} , all matrices belonging to pressure degrees of freedom into the matrix A^{pp} and all FE-coupling matrices into C^{up} , the system of linear equations for the unknown variables reads as follows:

$$\begin{bmatrix} A^{uu} & C^{up} & C_{BE}^S & 0 \\ C^{up^T} & A^{pp} & 0 & \frac{1}{j\omega} C_{BE}^{BF} \\ j\omega G S_v^{-1} C_{BE}^{S^T} & H S_p^{-1} C_{BE}^{BF^T} & H & -G \end{bmatrix} \begin{bmatrix} u^{FE} \\ p^{FE} \\ p^{BE} \\ v^{BE} \end{bmatrix} = \begin{bmatrix} r_{FE}^0 \\ 0 \\ r_{BE}^0 \end{bmatrix} \quad (18)$$

It is worth noting that the matrix on the left-hand side of Equation (18) is a square matrix although it is shown as a rectangular matrix. This is due to the fact that the BE-unknowns have been partitioned into pressure and normal velocity unknowns.

Instead of solving the entire non-symmetric system of linear equations (18) using an iterative solver, we propose the following approach, which can be regarded as a generalization of the approach using an impedance matrix Z proposed in [15].

The unknowns u^{FE} and p^{FE} can be eliminated from Equation (18) via

$$\begin{bmatrix} u^{FE} \\ p^{FE} \end{bmatrix} = -A_{FE}^{-1} C_{BE}^{FE} \begin{bmatrix} p^{BE} \\ v^{BE} \end{bmatrix} + A_{FE}^{-1} r_{FE}^0$$

As the matrix A_{FE} is implicitly frequency-dependent because of the dissipation effects occurring in the absorbing material, the standard modal reduction technique cannot be applied to eliminate the FE-unknowns. An alternative method of evaluating the complex eigenvectors and eigenvalues and an adapted modal reduction method that can be used instead of a direct solution can be found in [43]. However, here we are using a sparse direct solver to solve the symmetric and frequency-dependent system of linear equations $A_{FE}x = y$.

Injecting u^{FE} and p^{FE} into the last row of Equation (18) gives the sound pressure and velocity distribution at the boundary Γ_{BE} as follows:

$$pp = \underbrace{\begin{bmatrix} I & 0 \\ -S_p^{-1} C_{BE}^{BF^T} & A_{FE}^{-1} C_{BE}^{FE} \end{bmatrix}}_{=:C^p} \begin{bmatrix} p^{BE} \\ v^{BE} \end{bmatrix} + \underbrace{S_p^{-1} C_{BE}^{BF^T} A_{FE}^{-1} r_{FE}^0}_{=:pp^0}$$

$$vv = \underbrace{\begin{bmatrix} j\omega S_v^{-1} C_{BE}^{S^T} & A_{FE}^{-1} C_{BE}^{FE} \\ 0 & I \end{bmatrix}}_{=:C^v} \begin{bmatrix} p^{BE} \\ v^{BE} \end{bmatrix} - \underbrace{j\omega S_v^{-1} C_{BE}^{S^T} A_{FE}^{-1} r_{FE}^0}_{=:vv^0}$$

The vectors pp^0 and vv^0 exert an additional load on Γ_{BE} due to nodal forces and surface loads given at Γ_S , and these will contribute to the vector r_{BE}^0 alone, whereas the matrix $S_p^{-1} C_{BE}^{BF^T} A_{FE}^{-1} C_{BE}^{FE}$

can be regarded as a global impedance and $j\omega S_v^{-1} C_{BE}^S A_{FE}^{-1} C_{BE}^{FE}$ as a global admittance condition imposed on the fluid domain Ω_{BE} at the corresponding parts of its boundary Γ_{BE} . These two matrices form the counterpart to the local impedance or admittance boundary condition often introduced to approximate the presence of vibrating structures or absorbing materials in acoustic analyses.

Finally, the unknown variables p^{BE} and v^{BE} follow from the solution of

$$\begin{aligned} [HC^p - GC^v] \begin{bmatrix} p^{BE} \\ v^{BE} \end{bmatrix} &= r_{BE}^0 - Hpp^0 + Gvv^0 \\ A_{BE}x &= r_{BE} \end{aligned} \quad (19)$$

To solve this non-symmetric system of linear equations, the iterative solver GMRes [44] was applied. The convergence of this iterative solver was improved using a preconditioner [45] based on an incomplete LU-factorization [46] procedure. As neither the matrices C^p and C^v nor SDT^H and SDT^G are available explicitly, only the near-field matrices $H_{\mathcal{N}}$ and $G_{\mathcal{N}}$ can be used to calculate the preconditioner at an acceptable numerical cost. Therefore, only the matrix

$$\begin{bmatrix} H_{\mathcal{N}}^{pp} & -G_{\mathcal{N}}^{pv} \\ H_{\mathcal{N}}^{vp} & -G_{\mathcal{N}}^{vv} \end{bmatrix}$$

was factorized and used as a preconditioner. The symbol $H_{\mathcal{N}}^{pp}$ denotes the part of the matrix $H_{\mathcal{N}}$ corresponding to a part of the boundary Γ_{BE} where the sound pressure is the unknown quantity and $H_{\mathcal{N}}^{vp}$ denotes the part of the matrix $H_{\mathcal{N}}$ corresponding to a part of the boundary Γ_{BE} where the velocity is the unknown quantity of the BEM. The corresponding notation has been used for the matrix G .

The FE/FMBEM-coupling method presented here has been encoded at the LMA in Marseille using Fortran 90. This computer code, named AKUSPOR, is applicable to a wide range of industrial applications arising in the field of structural mechanics, sound propagation in fluids and absorbing materials and the coupling between these fields.

6. EXPERIMENTS AND NUMERICAL EXAMPLES

The present FE/FMBE-coupling method will be applied to calculate the absorption coefficient of the acoustic lining used in the large anechoic chamber at the LMA. In the second example, the numerical method presented will be applied to simulate the acoustic behavior of an entire anechoic chamber in the low-frequency range.

In the first step, a series of experiments was carried out in an impedance tube measuring $1.2 \times 1.2 \times 6 \text{ m}^3$ to obtain experimental data with which to check the quality of the numerical algorithm dealing with a problem of practical interest. In the second step, the numerical algorithm was used to calculate the absorption coefficient in the case of a configuration that could not be investigated experimentally. The main particularity of these measurements and numerical simulations is that the mounting of the acoustic lining has to be taken into account in order to obtain accurate results.

The acoustic lining in question consists of melamine wedges, the bottom part of which has a rectangular cross section measuring $0.3 \times 0.3 \text{ m}^2$. The wedges are 0.4 m in length and they have

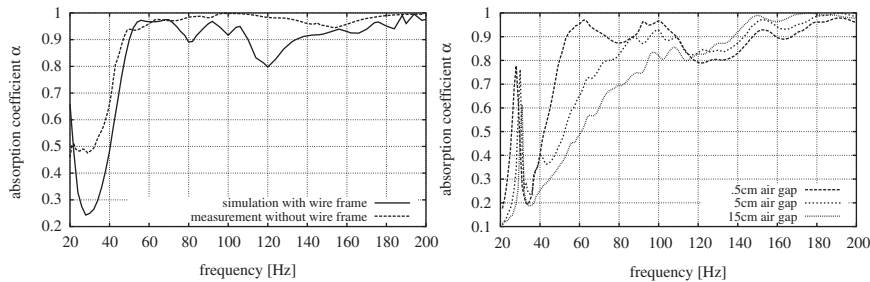


Figure 2. Influence of the mounting conditions on the absorption coefficient (left-hand side sub-figure). Absorption coefficients measured with air gaps of different sizes around the sample of the absorbing material (right-hand side sub-figure).

a tapering section 0.7 m in length. The wedges are held in place by an iron wire frame. To account for the mounting conditions of the acoustic lining in the anechoic chamber at LMA, the wire frame was also used when carrying out the impedance tube experiments. A sample of 3×3 wedges was chosen and the frame was screwed to three wooden bars, leaving an 11 cm air gap behind the sample. Wooden bars were assumed to be motionless, which was checked by measuring their displacement. The use of a sample of 3×3 wedges leaves an air gap of 15 cm around the melamine wedges. This prevents the occurrence of any lateral contact between the absorbing material and the iron wire frame and the walls of the impedance tube. This configuration is characterized by well-defined boundary conditions, which will reduce the sources of errors in the subsequent numerical analysis. To study the influence of the air gap around the sample, it was closed up using a multi-piece wooden frame. Three different configurations were investigated: (1) a wooden frame 14.5 cm in width, leaving an air gap of approximately 0.5 cm between the sample and the wooden frame; (2) a wooden frame 10 cm in width, leaving an air gap of 5 cm between the sample and the wooden frame; and (3) no wooden frame, leaving an air gap of 15 cm between the sample and the walls of the tube. The first configuration was installed and measurements were carried out. The wooden frame was then accordingly removed to obtain configurations 2 and 3 without changing the position of the sample of the absorbing material. The transfer function method [47–49] and a pure sine tone excitation were used to measure the acoustic properties of the sample. The absorption coefficients measured in the three configurations are shown in Figure 2. Reducing the air gap led to a significant increase in the absorption coefficient at low frequencies and to a slight decrease at frequencies above 120 Hz. Besides this quite well-known effect, an increase in the absorption coefficient was observed in the 80–110 Hz frequency range, which was attributable to longitudinal structural modes of the wedges.

It is worth pointing out the significant decrease in absorption observed in the 110–140 Hz frequency range. In this frequency range, as well as in the 70–90 Hz range, there exist no structural modes[‡] that might lead to additional absorption apart from that of the material itself. Hence, spreading out the structural modes of the wedges over the 70–150 Hz frequency range provides a possible means of improving the quality of the acoustic lining.

[‡]Longitudinal displacement of the wedges was measured using an MTI-2000 fiber-optic-based sensor.

The experiments described above were simulated using the FE/FMBE-coupling method presented here. The iron wire frame, the absorbing material and the air behind and around the bottom part of the wedges were modeled using the FEM and quadratic basis functions. Sound propagation in the impedance tube was modeled using the BEM and linear discontinuous basis functions. The acoustic sound source, a 40-cm-diameter loudspeaker, was simulated by a uniform normal surface velocity at the corresponding end of the tube. Parts of the meshed geometry (wedges, air gap, iron wire frame and part of the BE-surface mesh) are shown in Figure 3. The resulting linear system of equation consists of $N_{\text{FE}} = 120377$ FE and $N_{\text{BE}} = 10888$ BE-unknowns. A four-level FMM with a truncation length M equal to $M = 5, \dots, 18$ depending on the level of FMM and the excitation frequency was applied. The numerical solution required ≈ 2 Gb main memory.

As the material properties of the melamine foam are anisotropic as the result of the foaming processes, attention must be paid to the orientation of the material axis with respect to the wedge geometry. The wedges were cut out of raw melamine blocks in an unpredictable manner, but in the direction in which the material was foamed. However, the actual orientation of the material axes of the wedges used for these experiments could not be determined. To meet this specific configuration, the sample of 3×3 wedges was modeled by setting Young's modulus in the direction of the wedge length to the values given in Table I, taking three wedges at a time. The configuration chosen is shown on the left-hand side of Figure 3 where each of the three material orientations is indicated by a different number. To account for the structural damping occurring in the melamine foam, a complex Young's modulus $\tilde{E}_i = E_i(1 + 0.01j)$ was used. Numerical simulations were run on an SGI Origin3800 at the Center for Information Services and High Performance Computing of the Technische Universität Dresden, Germany. The iterative solver GMRes preconditioned with an $\text{ilut}(350, 1e-5)$ preconditioner [46] required between $n_{\text{iter}} = 800$ iterations at 20 Hz and $n_{\text{iter}} = 230$ iterations at 200 Hz to solve Equation (19) with a relative residual of $\varepsilon = 1.0e-6$. Without the preconditioner, $n_{\text{iter}} = 1700$ at 20 Hz and $n_{\text{iter}} = 1050$ at 200 Hz iterations were required.

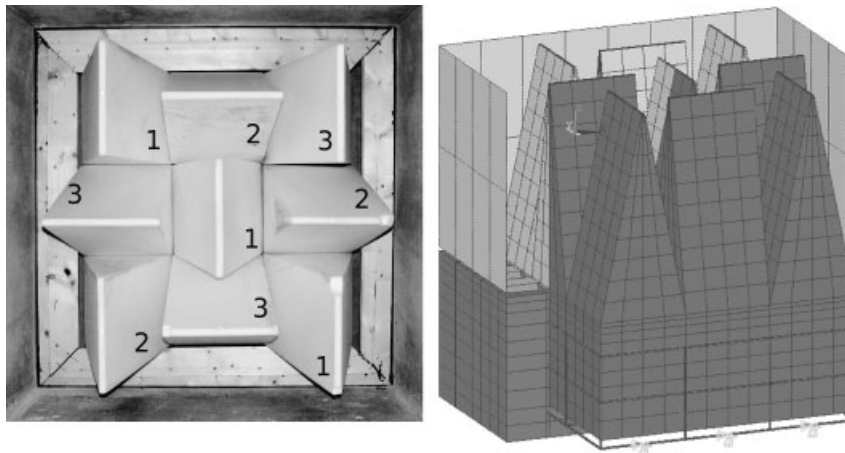


Figure 3. Photograph showing the position of the wedges and the wooden frame in the impedance tube (left-hand side figure). Numbering of the wedges indicates the three sets of material orientations in use. The meshed geometry of the melamine wedges and surrounding air and (parts of the) walls of the impedance tube are shown in the right-hand side figure.

Table I. Melamine material parameters used for the numerical simulations.

Young's modulus (N/m ²)			Shear modulus (N/m ²)			The Poisson ratio		
E_x	E_y	E_z	G_{xy}	G_{yz}	G_{xz}	ν_{xy}	ν_{xz}	ν_{yz}
0.30e6	0.22e6	0.50e6	0.10e6	0.08e6	0.21e6	0.44	0.26	0.19

Parameters were identified in impedance tube experiments using a $6 \times 6 \times 6 \text{ cm}^3$ sample glued to the sample-holder of a 10-cm-diameter impedance tube.

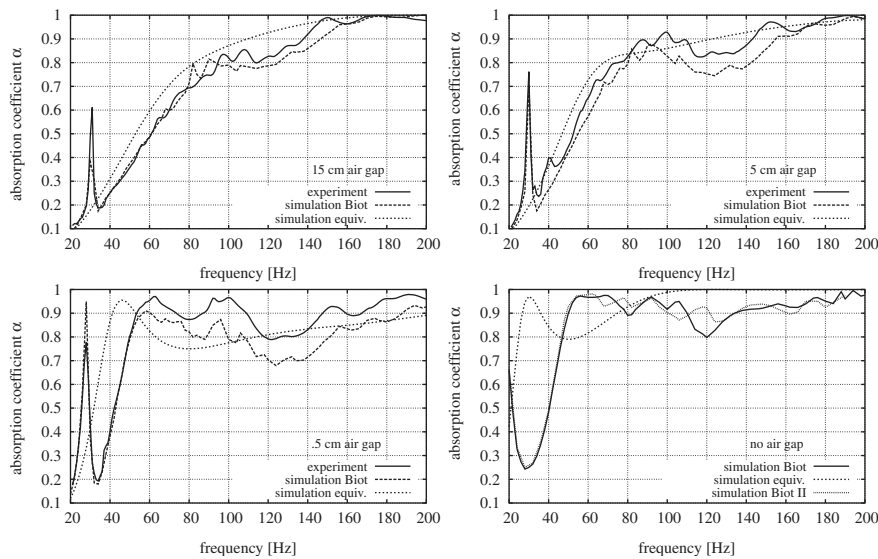


Figure 4. Comparisons between the measured and calculated absorption coefficients of the 3×3 sample of wedges with different air gap sizes. Numerical simulations were performed using Biot's theory and the equivalent fluid model to describe the behavior of the absorbing material.

The results of the numerical simulation were compared with the experimental data obtained with the three experimental configurations in Figure 4. Simulated and experimental data agree quite well over the entire frequency range, when Biot's theory was applied to model the absorbing material. However, the exact position of the resonance peaks could not be predicted in the case of the 15 cm air gap configuration. Nevertheless, the numerical model predicted the effects of the structural modes on the absorbing behavior of the sample quite accurately. Note that only using three orientations of the material axes yielded a set of structural modes in the 80–110 Hz frequency range as observed experimentally. Using an isotropic material for the melamine foam yields a single mode in that frequency range. In general, the simulation seems to have overestimated the stiffness of the melamine foam, which results in a slight shift of the absorption coefficient curve toward higher frequencies, whereas the absorption coefficients at higher frequencies were underestimated, possibly due to absorption by the wooden frame, which was not taken into account in the numerical model. The choice of material orientations may have been a further source in errors in the numerical simulation. Note that the absorption coefficients measured reflect the acoustic behavior of the wedges, the wooden frame and the remaining air gap. The lower right-hand

side sub-figure in Figure 4 shows the numerical results obtained on the 3×3 sample of wedges placed in an impedance tube measuring $0.9 \times 0.9 \text{ m}^2$, which reflects the properties of the melamine wedges placed in the anechoic chamber. The absorption coefficient of the acoustic lining sample was found to be acceptable in the 50–75 Hz frequency range. However, a significant decrease in the absorption coefficient was observed in the 110–170 Hz frequency range. This behavior of the melamine wedges contrasts with the results of the impedance tube experiment conducted without an iron wire frame (see left-hand side sub-figure of Figure 2) but is in good agreement with the results of measurements carried out in the anechoic chamber, where significant deviations from the free-field conditions were observed in this frequency range. Spreading out the structural modes of the wedges over the 110–170 Hz frequency range may reduce the decrease in the absorption coefficient observed with the present configuration. Structural modes were already partly spread out by randomly adopting the orientation of the wedges relative to the orientation of the material axes. The length of the wedges can also be varied to create a lining with a less strongly fluctuating absorption coefficient. Therefore, in each of the three material orientations, three wedges with different tapering section lengths of 0.6, 0.7 and 0.8 m were simulated numerically. The result of this simulation, labeled ‘simulation Biot II’, is given in the lower right-hand side sub-figure in Figure 4. The absorption coefficient of this sample shows weaker variations and a much less marked breakdown at a frequency of around 120 Hz. Hence, with almost the same quantity of absorbing material, a more efficient acoustic lining can be obtained. The flexibility of the proposed FE/FMBE-coupling method in terms of the geometric shape of the wedges means that this method provides an efficient means of designing acoustic linings with better performances.

It is worth noting that taking the frame of the melamine foam to be motionless, that is, using the equivalent fluid model instead of the complete Biot model, yields absorption coefficients (see Figure 4) that do not reflect the behavior of the melamine wedges, as the acoustic behavior of the melamine foam depends on the elastic frame.

After these preliminary investigations on the behavior of the acoustic lining in an impedance tube, numerical simulations were carried out on the entire anechoic chamber at the LMA. The aim of these numerical experiments was to predict the quality of the anechoic chamber in the low-frequency range. The quality of an anechoic chamber was defined here as the size of the region where the perturbations caused by reflections from the walls are smaller than 1.5-dB. This region will be referred to as the 1.5-dB region in what follows. At the large anechoic chamber at the LMA, this 1.5-dB region was determined experimentally in the 20–200 Hz frequency range. At higher frequencies, no significant perturbations were observed experimentally. The bounds of the 1.5-dB region measured with two source positions are given by the solid line in the two sub-figures in Figure 6.

The acoustic lining consists of 3720 melamine wedges held in place by means of an iron wire frame. In the simulations, each individual element of the lining was meshed using 24 Biot, four-fluid and 28 structural elements. With this FE-mesh of the absorbing material, 26 boundary elements were obtained. Figure 5 shows the meshed model for a single component of the acoustic lining. Linear basis functions were used for the domains Ω_B , Ω_F and Ω_S . To prevent locking effects, extra displacement shape functions were added to the linear basis functions of the Biot and structural elements and constant boundary elements were used.

The anisotropy of the melamine foam observed was accounted for in the same way as in the previous numerical example. Different material orientations were randomly distributed over the walls of the chamber. The model for the entire anechoic chamber consisted of $N_{FE} = 3.3e6$ FE-unknowns and $N_{BE} = 104\,172$ BE-unknowns. To store the Cholesky-factor L , 6.1 Gb of memory

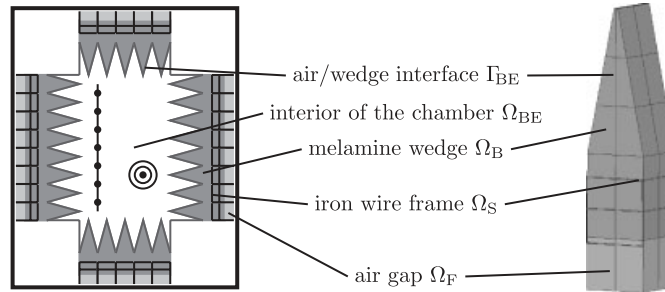


Figure 5. A geometric model of the anechoic chamber and the meshing of a single component of the acoustic lining.

Table II. Memory requirements (left-hand side sub-table) and computational resources required to obtain one matrix–vector product (right-hand side sub-table), using an 8-level FM algorithm.

Matrix	Memory (Gb)	CPU time		Flops		Flop rate (%)	
		(s)	(%)	(Mflops)	(%)		
L	6.1	Operation					
$H_{\mathcal{N}}$	2.3	BEM ILU SOL	5.9	6.2	372.2	4.9	15.6
$G_{\mathcal{N}}$	2.3	BEM MLFMA	29.4	30.8	2783.1	36.9	23.6
MLFMA	0.2	FEM $AX=B$	60.3	63.0	4386.0	58.2	18.2
GMRes(m)	6.1	Total	95.7	100.0	7541.3	100.0	19.7
Sum	17.0						

The last column in the right-hand side table gives the performance of the algorithm versus the peak performance of the computer processor.

was required. This corresponds to a band matrix with an average bandwidth of 133. A single 2.6 GHz AMD Opteron-processor at the Linux Networx PC-Farm of the Technische Universität Dresden, Germany, took ≈ 35 min to calculate the factorization. The BE part of the entire numerical simulation required 5 Gb main memory and the evaluation of the matrices $H_{\mathcal{N}}$ and $G_{\mathcal{N}}$ took 1 h on the above-mentioned computer. The length M of the series expansion in Equation (17) was equal to $M=5, \dots, 24$ depending on the frequency. The computational resources, the time and the number of floating point operations required to perform a matrix–vector product are given on the right-hand side of Table II. The results given in this table show that the numerical complexity and the memory required were more or less equally allocated to the two numerical methods. But the number of matrix–vector products required by the preconditioned iterative solver to solve Equation (19) with a residual of $\varepsilon = 1.0e-6$ was highly frequency dependent. The total solution time per frequency was 25 h at 20 Hz, 12 h at 40 Hz and 4 h at 80–200 Hz, which corresponds to 4100, 2100 and 330 iterations, respectively, due to the slow convergence of the iterative solver although the preconditioner was applied. The decrease in the number of iterations with the frequency may be attributable to the fact that at higher frequencies, the acoustic lining is more absorbent than at lower frequencies. It has been established previously (see [50, 51]) that the absorption significantly affects the number of iterations.

In Figure 6, the results of the numerical simulations are compared with the experimental data. The 1.5-dB region of the large anechoic chamber at the LMA was determined using two source positions. The bounds of the 1.5-dB region measured are indicated in Figure 6 by a solid line. Note that the perturbations are higher than the allowed 1.5-dB in the 110–160 Hz frequency range.

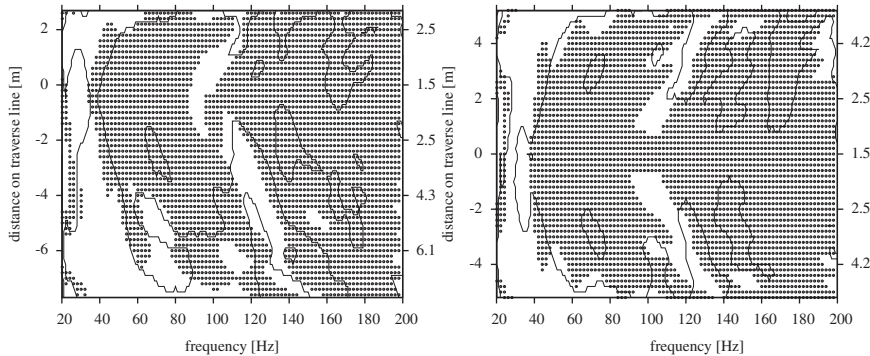


Figure 6. The 1.5-dB region (solid line) measured superimposed on the results of the numerical simulation (dots) in the case of two sound source positions.

Comparisons with the results of the impedance tube experiments on the acoustic lining show that this frequency range corresponds to the frequency range in which a breakdown of the absorption coefficient occurred in the one-dimensional experiments.

Results of the numerical simulation are given in Figure 6. Each frequency/position pair predicted to belong to the 1.5-dB region is indicated by a solid dot. Good agreement with the experimental data can be observed up to at least 100 Hz. At higher frequencies a slight frequency shift in the numerical results was observed. This may be due to insufficient spatial discretization. The imperfections of the acoustic lining in the 110–160 Hz frequency range are correctly mapped, but their effects on the 1.5-dB region of the chamber is somehow underestimated, especially in the 140–160 Hz frequency range. The computation time was less than 12 h at frequencies above 40 Hz, and thus parametric studies on the influence of some parameters of the acoustic lining on the performance of an anechoic chamber can be carried out using current computers. The flexibility of the FE/FMBE-coupling method means that it is possible to vary the shape, size and the material properties of each individual lining component with almost no additional effort.

7. CONCLUSIONS

An FE/BE-coupling method is presented here for simulating fluid/structure interaction problems of practical interest, where arbitrarily shaped objects are embedded in a homogeneous fluid. The FEM was used to model the structural and absorbing material parts of the problem. The flexibility of this method in terms of the geometry, boundary conditions and material behavior makes it applicable to a large range of industrial problems. To avoid the need to mesh the fluid domain, the FMBEM was used to model the sound propagation in the surrounding homogeneous fluid.

The resulting FE/FMBE-coupling method turned out to be a highly flexible numerical tool, as it benefits from the advantages of both numerical methods. However, the iterative solution of the system of linear equations is often the most time-consuming part of the simulation. The development of a more suitable preconditioner is urgently required and this problem is now being addressed in an ongoing research project.

The FE/FMBE-coupling method presented here was used to calculate the absorption coefficient of an acoustic lining and to simulate the acoustic behavior of an entire anechoic chamber.

ACKNOWLEDGEMENTS

This research was financed by a grant from the German Research Foundation. Numerical simulations were run on a Linux Network PC-Farm at the Center for Information Services and High Performance Computing at the Technische Universität Dresden, Germany. The author wishes to thank C. Kern who made the experimental data on the anechoic chamber available.

REFERENCES

1. Zienkiewicz OC, Taylor RL. *The Finite Element Method*, vols I–II. Butterworth-Heinemann: Oxford, 2000.
2. Ihlenburg F. *Finite Element Analysis of Acoustic Scattering*. Applied Mathematical Sciences, vol. 132. Springer: Berlin, Heidelberg, New York, 1998.
3. Biot MA. Theory of propagation of elastic waves in a fluid-saturated porous solid. I. Low-frequency range. *Journal of the Acoustical Society of America* 1956; **28**(2):168–178.
4. Allard J-F. *Propagation of Sound in Porous Media. Modelling Sound Absorbing Materials*. Elsevier: London, New York, 1993.
5. Panneton R, Atalla N. An efficient finite element scheme for solving the three-dimensional poroelasticity problem in acoustics. *The Journal of the Acoustical Society of America* 1997; **101**(6):3287–3298.
6. Atalla N, Panneton R, Deberge P. A mixed pressure–displacement formulation for poroelastic materials. *Journal of the Acoustical Society of America* 1998; **104**(3):1444–1542.
7. Schanz M, Pryl D. Dynamic fundamental solutions for compressible and incompressible modeled poroelastic continua. *International Journal of Solids and Structures* 2004; **41**(15):4047–4073.
8. Tanneau O, Lamary P, Chevalier Y. A boundary element method for porous media. *The Journal of the Acoustical Society of America* 2006; **120**(3):1239–1251.
9. Morand HJ-P, Ohayon R. *Fluid Structure Interaction*. Wiley: Chichester, Paris, 1995.
10. Harari I, Grosh K, Hughes TJR, Malhotra M, Pinsky PM, Stewart JR, Thompson LL. Recent development in finite element methods for structural acoustics. *Archives of Computational Methods in Engineering* 1996; **3**(2–3):131–309.
11. Fischer M, Gaul L. Fast BEM-FEM mortar coupling for acoustic-structure interaction. *International Journal for Numerical Methods in Engineering* 2005; **62**(12):1677–1690.
12. Bettess P. *Infinite Elements*. Penshaw Press: Sunderland, 1992.
13. Burnett DS. A three dimensional acoustic infinite element based on a prolate spheroidal multipole expansion. *Journal of the Acoustical Society of America* 1994; **96**:2798–2816.
14. Wu TW (ed.). *Boundary Element in Acoustics: Fundamentals and Computer Codes*. WIT Press: Southampton, 2000.
15. Everstine GC, Henderson FM. Coupled finite element/boundary element approach for fluid–structure interaction. *Journal of the Acoustical Society of America* 1990; **87**(5):1938–1947.
16. Chen ZS, Hofstetter G, Mang HA. A Galerkin-type BE–FE formulation for elasto-acoustic coupling. *Computer Methods in Applied Mechanics and Engineering* 1998; **152**(1–2):147–155.
17. Fritze D, Marburg S, Hardtke H-J. FEM-BEM-coupling and structural-acoustic sensitivity analysis for shell geometries. *Computers and Structures* 2005; **83**(2–3):143–154.
18. Zhou Q, Joseph PF. A numerical method for the calculation of dynamic response and acoustic radiation from an underwater structure. *Journal of Sound and Vibration* 2005; **283**(3–5):853–873.
19. Atalla N, Sgard F, Amedin CK. On the modeling of sound radiation from poroelastic materials. *Journal of the Acoustical Society of America* 2006; **120**(4):1990–1995.
20. Beylkin G, Coifman R, Rokhlin V. Fast wavelet transforms and numerical algorithms I. *Communications in Pure and Applied Mathematics* 1991; **44**:141–183.
21. Hackbusch W. A sparse matrix arithmetic based on H-matrices. Part I: introduction to H-matrices. *Computing* 1999; **62**:89–108.
22. Bebendorf M, Rjasanov S. Adaptive low-rank approximation of collocation matrices. *Computing* 2003; **70**:1–24.
23. Bespalov A. On the usage of a regular grid for implementation of boundary integral methods for wave problems. *Russian Journal of Numerical Analysis and Mathematical Modelling* 2000; **15**(6):469–488.
24. Hackbusch W, Nowak ZP. On the fast matrix multiplication in the boundary element method by panel clustering. *Numerische Mathematik* 1989; **54**:463–491.

25. Greengard L, Rokhlin V. A fast algorithm for particle simulations. *Journal of Computational Physics* 1987; **73**(2):325–348.
26. Biot MA. Theory of propagation of elastic waves in a fluid-saturated porous solid. II. Higher frequency range. *Journal of the Acoustical Society of America* 1956; **28**(2):179–191.
27. Johnson DL, Koplik J, Dashen R. Theory of dynamic permeability and tortuosity in fluid-saturated porous media. *Journal of Fluid Mechanics* 1987; **176**:379–401.
28. Champoux Y, Allard J-F. Dynamic tortuosity and bulk modulus in air-saturated porous media. *Journal of Applied Physics* 1991; **70**(4):1975–1979.
29. Ohayon R, Soize C. *Structural Acoustics and Vibration*. Academic Press: New York, 1998.
30. Babuška I, Szabó B. *Finite Element Analysis*. Wiley: New York, Chichester, 1991.
31. Colton D, Kress R. *Integral Equation Methods in Scattering Theory*. Wiley: New York, 1983.
32. Burton AJ, Miller GF. The application of integral equation methods to the numerical solution of some exterior boundary-value problems. *Proceedings of the Royal Society of London, Series A* 1971; **323**:201–220.
33. Amini S. On the choice of the coupling parameter in boundary integral formulations of the exterior acoustic problem. *Applicable Analysis* 1990; **35**:75–92.
34. Pyl D, Clouteau L, Degrande G. A weakly singular boundary integral equation in elastodynamics for heterogeneous domains mitigating fictitious eigenfrequencies. *Engineering Analysis with Boundary Elements* 2004; **28**(12):1493–1513.
35. Tadeu AJB, Godinho L, Santos P. Performance of the BEM solution in 3D acoustic wave scattering. *Advances in Engineering Software* 2001; **32**(8):629–639.
36. Marburg S, Schneider S. Influence of element types on numeric error for acoustic boundary elements. *Journal of Computational Acoustics* 2003; **11**(3):363–386.
37. Zhang X. Coupling FEM and discontinuous BEM for elastostatics and fluid–structure interaction. *Engineering Analysis with Boundary Elements* 2002; **26**(8):719–725.
38. Gumerov NA, Duraiswami R. *Fast Multipole Methods for the Helmholtz Equation in Three Dimensions*. Elsevier: Oxford, U.K., 2005.
39. Abramowitz M, Stegun IA. *Handbook of Mathematical Functions*. Dover: New York, 1965.
40. Darve E. The fast multipole method I: error analysis and asymptotic complexity. *SIAM Journal on Numerical Analysis* 2001; **38**(1):98–128.
41. Schneider S. Application of fast methods for acoustic scattering and radiation problems. *Journal of Computational Acoustics* 2003; **11**(3):387–401.
42. Debergue P, Panneton R, Atalla N. Boundary conditions for the weak formulation of the mixed (u, p) poroelasticity problem. *Journal of the Acoustical Society of America* 1999; **106**(5):2383–2390.
43. Dazel O, Sgard F, Lamarque C-H. Application of generalized complex modes to the calculation of the forced response of three-dimensional poroelastic materials. *Journal of Sound and Vibration* 2003; **268**(3):555–580.
44. Saad Y, Schultz MH. GMRES: a generalized minimal residual algorithm for solving nonsymmetric linear systems. *SIAM Journal on Scientific and Statistical Computing* 1986; **7**(3):856–869.
45. Schneider S, Marburg S. Performance of iterative solvers for acoustic problems. Part II: acceleration by ILU-type preconditioner. *Engineering Analysis with Boundary Elements* 2003; **27**(7):751–757.
46. Saad Y. ILUT: a dual threshold incomplete LU factorization. *Numerical Linear Algebra with Applications* 1994; **1**(4):387–402.
47. ISO 10534-2:1998. *Acoustics—Determination of Sound Absorption Coefficient and Impedance in Impedance Tubes—Part 2: Transfer-function Method*, 1998.
48. Chung JY, Blaser DA. Transfer function method of measuring in-duct acoustic properties. I. Theory. *Journal of the Acoustical Society of America* 1980; **68**(3):907–913.
49. Chung JY, Blaser DA. Transfer function method of measuring in-duct acoustic properties. II. Experiment. *Journal of the Acoustical Society of America* 1980; **68**(3):914–921.
50. Yasuda Y, Sakamoto S, Kosaka Y, Sakuma T, Okamoto N, Oshima T. Numerical analysis of large-scale sound fields using iterative methods. Part I: application of Krylov subspace methods to boundary element analysis. *Journal of Computational Acoustics* 2007; **15**, accepted.
51. Marburg S, Schneider S. Performance of iterative solvers for acoustic problems. Part I: solvers and effect of diagonal preconditioning. *Engineering Analysis with Boundary Elements* 2003; **27**(7):727–750.